

# CYCLING SIGNATURES: IDENTIFYING OSCILLATIONS FROM TIME SERIES USING ALGEBRAIC TOPOLOGY

ULRICH BAUER<sup>1,2</sup>, DAVID HIEN<sup>1</sup>, OLIVER JUNGE<sup>1</sup>  
AND KONSTANTIN MISCHAIKOW<sup>3</sup>

**ABSTRACT.** Recurrence is a fundamental characteristic of complicated deterministic dynamical systems. Understanding its structure is challenging, especially if the system of interest has many degrees of freedom so that visualizations of trajectories are of limited use. To analyze recurrent phenomena, we propose a computational method to identify oscillations and the transitions between them. To this end, we introduce the concept of *cycling signature*, which is a topological descriptor of a trajectory segment. The advantage of a topological approach, in particular in an application setting, is that it is robust to noise. Cycling signatures are computable from data and provide a comprehensive global description of oscillations through their statistics over many trajectory segments. We demonstrate this through three examples. In particular, we identify and analyze six oscillations in a four-dimensional system with a hyperchaotic attractor.

## 1. INTRODUCTION

A fundamental characteristic of complex deterministic dynamics is recurrence; typical trajectories repeatedly attain states close to previously observed states. A natural approach to characterizing this recurrence is to identify oscillations. For example, simple chaotic dynamics, e.g., horseshoes, is often described in terms of a scaffolding based on periodic orbits [11]. The advantage of periodic orbits is that, at least abstractly, they are simple objects - a closed trajectory that goes around a ‘hole’. However, in the context of data driven dynamics they are difficult to identify, especially if the data has noise.

The contribution of this paper (see Section 3 for details) is to introduce the concept of *cycling signatures*, which assign to given time series data  $\Gamma$  a vector space  $V(\Gamma)$  of possible oscillations, with the property that for any segment  $\gamma$  of  $\Gamma$ ,  $V(\gamma)$  is a subspace of  $V(\Gamma)$ .

Conceptually, a cycling signature is meant to capture cycling motion, e.g., a periodic orbit, by identifying ‘holes’ in the data. The advantage of this approach is that algebraic topology provides well established robust dimension independent tools to identify and quantify these ‘holes’ [10, 9, 3, 22]. These tools allow us to compute a vector space with dimension equal to the number of holes in the data set. While the dimension of a vector space equals the number of basis elements, in general, there is no unique or canonical choice of basis. The same is true for our cycling signatures: given a segment of the time series  $\gamma$ , the dimension of  $V(\gamma)$ , called the *cycling rank* of  $\gamma$ , indicates the number of linearly independent (as measured by a first homology group) ‘holes’ that  $\gamma$  wraps around, but an identification of the specific ‘holes’ would still depend on a choice of basis. Nevertheless, valuable insights into the structure of recurrence of a dynamical system can be gained, without making any choice of basis, by analyzing the cycling signatures of a large number of segments. The resulting information is

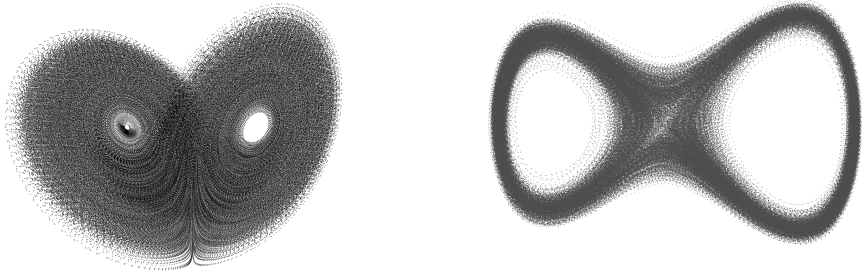


**Figure 1.** Time series for Lorenz (left) and stochastically perturbed double well (right).

quantitative in nature and can be interpreted without detailed knowledge of algebraic topology. In particular the computational results in Section 2 can be interpreted with the informal description of the cycling signature provided thus far. Furthermore, these insights can be obtained without having to visualize the data, an obvious advantage for higher dimensional systems.

## 2. UTILITY OF CYCLING SIGNATURES

To demonstrate the utility of cycling signatures, we consider three systems: the Lorenz system with the classical parameters [14], a perturbed Hamiltonian system derived from a scalar potential with two local minima (*the double well system*) and the Dadras system [7], a four-dimensional system with a hyperchaotic attractor (for detailed descriptions of the systems, see Appendix B). The first two systems are chosen to allow the reader to gain intuition via visualization. The third system is chosen to emphasize that this visualization is not necessary.

For each system, we generate a collection of cycling signatures as follows (see Appendix B for details). First, we generate a single long (multivariate) time series  $\Gamma = \{x(t_n) \mid n = 1, \dots, N\} \subset \mathbb{R}^d$  by numerically integrating the system, see Fig. 1 for the time series used for the Lorenz and double well systems. Second, we subsample short time series segments  $\gamma = \{x(t_n), \dots, x(t_{n+k})\}$  and compute their cycling signature. In our examples, we sample 1000 segments of length  $L$  for time span parameters  $L \in \{10, 20, \dots, 1000\}$ .

In this way, we obtain  $100 \times 1000$  cycling signatures for each system. Each signature is a subspace of the vector space  $V(\Gamma)$ , which for Lorenz is two-dimensional, for the double well is three-dimensional, and for Dadras is five-dimensional.

**Cycling rank.** The most direct information is summarized in the distribution of cycling ranks as a function of the segment time span, see Fig. 2.

In all three figures, any sufficiently long segment has positive cycling rank, which implies that our method detects cycling motion. Furthermore, the time point at which the number of rank 0 segments begins to decrease suggests the minimal time of cycling (Lorenz 60; Double well 80; Dadras 40) and the time point at which there are no rank 0 segments indicates how long trajectories can go before cycling is detected (Lorenz 300; Double well 230; Dadras 200).

**Rank 1 signatures.** Segments with rank 1 are of particular interest as they express a single type of cycling motion, which is uniquely identified by its signature. We identify

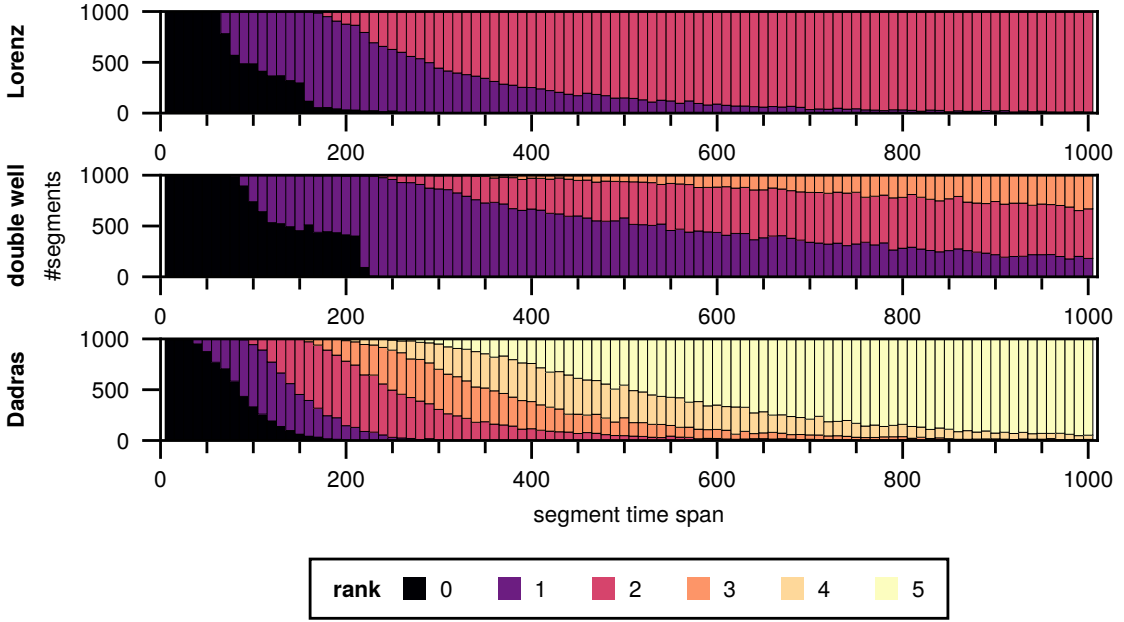


**Figure 2.** Distribution of cycling ranks for segments of different time lengths. Each plot consists of stacked barplots (one for each value of  $L$ ) showing the distribution of cycling ranks for the sampled segments. In all three plots, rank zero dominates for short lengths while long segments eventually attain the maximal possible rank of the system (i.e.  $\dim V(\Gamma)$ ).

an *oscillation* as a frequent signature of rank 1 segments. Fig. 3 shows the distributions of rank 1 signatures in the example datasets. This reveals that there are three oscillations in the Lorenz system, three in the double well system, and six in the Dadras system. Note that this observation is not in conflict with the fact that Lorenz and Dadras systems have two and five dimensional spaces  $V(\Gamma)$ , as the rank 1 signatures may be linearly dependent.

The smallest time span for which a particular oscillation appears allows us to infer information about the duration of the oscillations. Both Lorenz and double well possess two shorter and one longer oscillation (Lorenz: 70, 70, 160; double well: 70, 90, 210), whereas Dadras possesses four shorter ( $v_1-v_4$ ) and two longer oscillations ( $v_5, v_6$ ), with time spans approximately 40 and 80.

**2.1. Higher rank signatures.** Longer time spans lead to segments that experience more complicated cyclic behavior. This is captured by higher rank signatures. Again, the signature itself does not reveal which cycling motions gives rise to it since vector spaces do not canonically decompose into one-dimensional subspaces. However, frequent higher rank signatures can still be used to relate lower rank signatures with each other via subspace inclusion.

Of particular interest is the case of rank 2 segments (see Fig. 4). A segment which visits exactly two different rank 1 oscillations has a rank 2 signature which is spanned by the two rank 1 signatures. Conversely, there cannot be direct transitions between two specific rank 1 oscillations if there is no rank 2 signature that contains the signatures of

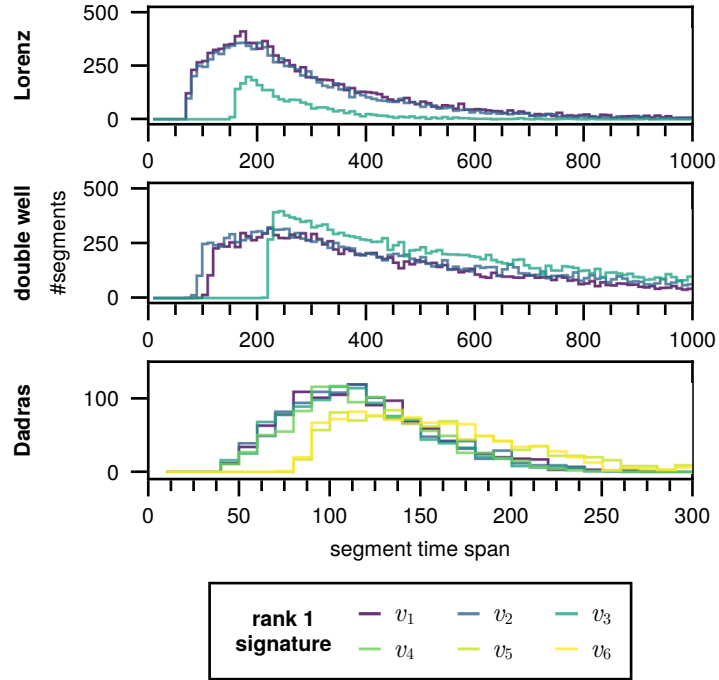


**Figure 3.** Distribution of rank 1 signatures for segments of different time spans. For double well and Dadras, we omit some additional signatures which appear very infrequently.

these rank 1 oscillations. This allows us to rule out direct transitions between certain oscillations.

In the Lorenz system we observe a two-dimensional space  $V(\Gamma)$ , therefore all rank 2 segments have the same signature  $V(\Gamma)$ , and all three of the frequent rank 1 signatures are subspaces of this signature (see Fig. 5). Algebraically, the long oscillation  $v_3$  in Lorenz is therefore a linear combination of the two short oscillations  $v_1$  and  $v_2$ . These results match our intuitive understanding of the dynamics on the Lorenz attractor, consisting of two wings with outward spiraling oscillations. The third oscillation is the “sum” of the oscillations on the individual wings and traces a figure 8 along both wings. Visualizations of segments that realize the three oscillations are shown in Appendix C.

In the other two systems, rank 2 segments provide deeper insight into the transitions between oscillations.

We cannot rule out any transition between the three prominent oscillations in the double well system. To see this, note that the statistics of the rank 2 signatures of double well, depicted in Fig. 4, reveal three prominent rank 2 signatures. It can be seen in Fig. 5 that any pair of rank 1 signatures is contained in a rank 2 signature (for example  $v_1$  and  $v_2$  are contained in  $w_3$ ).

For transitions that occur we obtain quantitative statements. As can be seen from Fig. 4, the signatures  $w_1$  and  $w_2$  appear much more frequently than  $w_3$ . The inclusion graph reveals that  $w_1$  and  $w_2$  contain the long oscillation  $v_3$  and one of the short oscillations  $v_1$  and  $v_2$ , whereas  $w_3$  contains both of the two short oscillations. An interpretation of this is that transitions between the short oscillations is less likely than transitions involving the long oscillation.

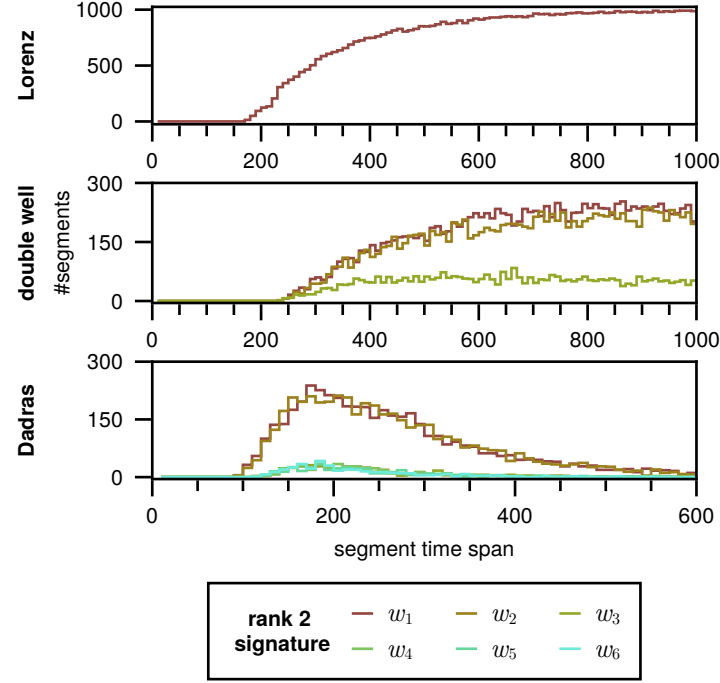


**Figure 4.** Distribution of rank 2 signatures in the example systems.

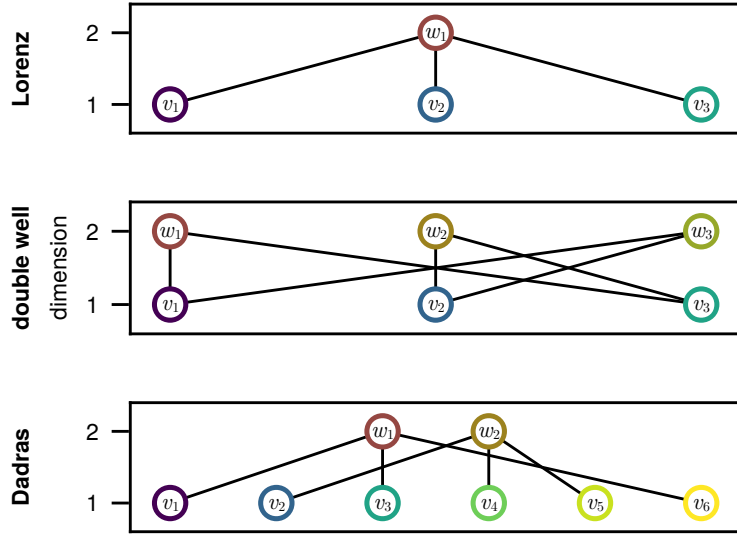


**Figure 5.** Inclusion graphs. In each plot, the nodes in the bottom and top rows correspond to frequent rank 1 and 2 signatures, respectively. Node colors correspond to the ones in Fig. 3 and Fig. 4. An edge indicates that the rank 1 signature is a subspace of the rank 2 signature.

In the Dadras system, we detect two prominent rank 2 signatures which organize the six oscillations into two clusters. These are defined by  $w_1$  and  $w_2$ , and consist of  $v_1, v_3, v_6$  and  $v_2, v_4, v_5$ , i.e., each contains two of the shorter and one of the longer oscillations. Note that  $w_1$  and  $w_2$  are disjoint, therefore direct transitions between oscillations in the same cluster are frequent while direct transitions between oscillations from different clusters are rare.

**Distinguishing the Lorenz, double well, and Dadras systems via cycling signatures.** Visually, there are similarities between the time series from Lorenz and the double well system (see Fig. 1); they both have two centers of rotation ('holes') around which trajectories oscillate. The dimensions of  $V(\Gamma)$  differ (2 for Lorenz, 3 for double well), but in and of itself this does not necessarily imply significant differences in the dynamics. However, we can quantify differences using the statistics of cycling signatures.

Fig. 3 shows that the Lorenz system has two prominent oscillations with similar length-frequency profiles, suggesting both oscillations occur with equal frequency. The double well system also has two prominent oscillations. In the length-frequency profiles, one appears before the other (70 vs. 90), suggesting that the two are of slightly different lengths of oscillation. In both systems, there is a third oscillation appearing at approximately twice the length of the other oscillations. In the Lorenz system this oscillation is observed infrequently, whereas in the double well system this third oscillation dominates in frequency once it appears at a time scale of 210. In summary, cycling signatures recover the similar structure of oscillations in the systems while also detecting quantitative differences.

As indicated in Fig. 2 the Dadras system possesses six oscillations while the other two systems only have three. In addition, the rank-frequency profiles (see Fig. 3) show that both Lorenz and double well have clear thresholds where oscillations appear, while in Dadras no such threshold can be determined.

**Cycling Signatures detect and classify oscillations in the Dadras system.** The Dadras system is a 4d system of ordinary differential equations, which appears to exhibit a (hyper)chaotic attractor [7]. As the system is four-dimensional, visualization is limited to projections that necessarily omit some spatial information. Cycling signatures allow us to analyze oscillations in the Dadras system without visualizations.

As indicated above, Fig. 3 indicates six oscillations; four shorter and two longer oscillations share similar length-frequency profiles. Our analysis of rank two segments (see Fig. 5) reveals that these are organized in two Lorenz-like clusters, each of which comprises two short and one long oscillation with the longer oscillation being a linear combination of the shorter ones.

### 3. MATHEMATICS OF CYCLING SIGNATURES

Conceptually, we assume that the dynamics of interest is generated by a differential equation whose solutions can be represented by a smooth flow, i.e., a differentiable function  $\Phi: \mathbb{R} \times X \rightarrow X$  such that  $\Phi(0, x) = x$  and  $\Phi(t + s, x) = \Phi(t, \Phi(s, x))$  for all times  $t, s \in \mathbb{R}$  and all points  $x$  in the *phase space*  $X$ .

For simplicity, we furthermore assume that the input for our approach is a single (long) time series, sampled from this dynamical system. More precisely, we assume

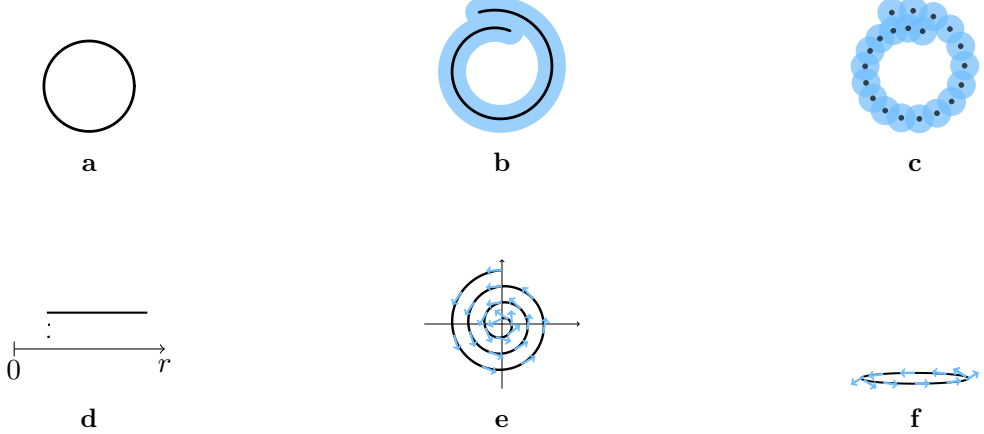


**Figure 6.** Illustrations for cycling definition. a: A periodic orbit is a topological circle. b: Almost periodic segment (black) with thickening (blue). c: Almost periodic time series segment (black) with thickening (blue). d: Barcode for the point cloud in c. e: Spiral sink. f: “Squished” periodic orbit.

the existence of an increasing sequence of times  $(t_i)_{i=1}^N$  which define a time series  $\Gamma = \{x(t_i) \mid i = 1, \dots, N\}$  via

$$x_i = x(t_i) = \Phi(x_0, t_i),$$

where  $x_0$  is some given initial point. A *segment* of  $\Gamma$  is a consecutive subsequence  $x_k, x_{k+1}, \dots, x_\ell$  for some  $k \leq \ell$ . The *time span* of a segment is  $t_\ell - t_k$ . The goal in the following is to associate each segment with a signature which identifies and classifies the cycling motions of the segment.

**Identification of Cycling Segments.** Our approach is motivated by the observation that homology [16] identifies periodic orbits. More precisely, suppose we are given a fragment  $\gamma = \Phi([a, b], x)$  of the orbit through some  $x \in X$ . Then  $\gamma$  contains a periodic orbit if and only if it is topologically equivalent to a circle, which in turn is the case if and only if  $H_1(\gamma) \neq 0$ . Since periodic orbits represent the simplest examples of oscillations, we generalize this observation to identify cycling.

Straightforward application of homology is met by conceptual and practical difficulties since both the non-periodicity as well as the finiteness of the given data automatically lead to trivial homology. We address both issues by replacing (the point cloud of) a segment  $\gamma = \{x(t_k), x(t_{k+1}), \dots, x(t_l)\}$  with its  $r$ -thickening defined by

$$(1) \quad \gamma^r = \{x \in X \mid d(x, \gamma) < r\},$$

where  $d$  is a metric on  $X$ . We declare that we have identified cycling if  $H_1(\gamma^r) \neq 0$  for a suitably chosen  $r \geq 0$ . This can be seen in Fig. 6b in the context of a closed fragment of an orbit  $\Phi([a, b], x)$  and in Fig. 6c in the context of a segment  $\gamma$  where a thickening (blue) of the original information (black) generates nontrivial  $H_1$ .

Next, we discuss the metric space used for the thickening. A meaningful distance of points from dynamic data should incorporate not only spatial, but also directional information. We realize this by lifting the data to the unit tangent bundle.

The tangent bundle  $T\mathbb{R}^d$  of  $\mathbb{R}^d$  can be described as the set of tuples  $(p, v) \in \mathbb{R}^d \times \mathbb{R}^d$  where  $p$  corresponds to a point in  $\mathbb{R}^d$  and  $v$  to the velocity of a curve through  $p$ . Since we are only interested in direction and not speed, we normalize the second component

and pass to the unit tangent bundle, which, for  $\mathbb{R}^d$ , is described by

$$\text{UTB}(\mathbb{R}^d) = \mathbb{R}^d \times S^{d-1} = \{(x, v) \in T\mathbb{R}^d \mid \|v\| = 1\}.$$

Any point  $x \in X$  that is not an equilibrium point of  $\Phi$  has an associated nonzero tangent vector  $v(x) = \frac{d}{dt}\Phi(t, x)|_{t=0}$ . Let  $X_0$  be the set of equilibria of  $\Phi$  and consider the section

$$(2) \quad \rho: X \setminus X_0 \rightarrow \text{UTB}(X), \quad x \mapsto (x, v(x)/\|v(x)\|)$$

of the unit tangent bundle induced by the flow. Instead of taking the distance between two points  $x, y \in X$  directly, we can now consider the distance between  $\rho(x)$  and  $\rho(y)$  which incorporates spatial as well as directional information.

To account for the normalization in the directional component, it is necessary to pass to an appropriate metric. We have no universal answer for what appropriate is and, therefore, introduce a parametrized family of unit tangent bundle metrics

$$d_C((p, v), (q, w)) = \max \{\|p - q\|_2, C\|v - w\|_2\}.$$

With a suitably selected constant  $C$ , thickenings of the segments in Fig. 6e and Fig. 6f have one dimensional  $H_1$  which corresponds to the oscillation around the origin.

Clearly, the choice of the thickening parameter  $r$  plays a significant role in our identification of oscillations. To address this we apply persistent homology [10, 9, 3, 22] to obtain a barcode decomposition of  $H_1(\gamma^\bullet)$  where  $\gamma^\bullet = \{\gamma^r\}_{r \geq 0}$  is the filtration. The barcode (a multiset of intervals) provides a representation from which the number of one-dimensional holes and the scales at which they appear and disappear can be read off for all choices of  $r$ . We adopt the (standard) heuristic that long bars identify meaningful cycling. Returning to the example of Fig. 6c, the associated barcode, shown in Fig. 6d, consists of three bars; two short bars that are not associated with meaningful dynamics and a long bar which corresponds to the hole in the center of the blue region.

**Definition 1.** A segment  $\gamma$  is *cycling* if  $H_1(\gamma^\bullet) \neq 0$  where the thickenings are with respect to a suitable metric  $d_C$ .

**Classification of Cycling Segments.** Recall that we view an oscillation as a collection of similar cycling segments. To organize these, we again make use of algebraic topology.

In order to compare segments, we consider the homology of a joint comparison space. A comparison space is a neighborhood  $Y$  of  $\rho(\Gamma)$ , where  $\rho$  is as in (2). For any segment  $\gamma$  of  $\Gamma$ , and  $r > 0$  small enough, we have an inclusion map  $i_{\gamma, r}: \rho(\gamma^r) \rightarrow Y$  which induces a map  $H_1(i_{\gamma, r}): H_1(\rho(\gamma)^r) \rightarrow H_1(Y)$  in homology. The image of this map defines a subspace  $\text{im } H_1(i_{\gamma, r})$  of  $H_1(Y)$ . We compare different cycling segments by their induced subspaces of  $H_1(Y)$ .

To illustrate this idea, consider the time series in Fig. 7. For simplicity, we disregard the unit tangent bundle (for the metric  $C = 0$ ) and let the union of the boxes in the figure be the comparison space  $Y$ . Since  $Y$  has two holes, we have  $\dim H_1(Y) = 2$ . Four orbit segments are highlighted: a green segment  $\gamma_g$  and a purple segment  $\gamma_p$  which only loop around the left hole in the complex, a yellow segment which only loops around the right hole in the complex, as well as a blue segment  $\gamma_b$  which orbits the right and the left hole.

Let  $r > 0$  be the thickening parameter of the blue, purple, and green segments. Each of these has the topology of a circle and therefore one-dimensional  $H_1$  where

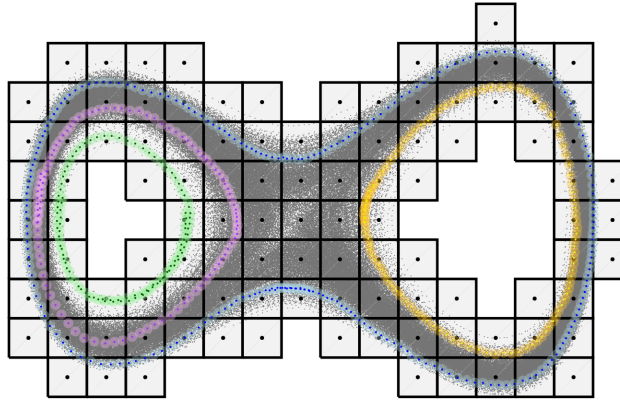


**Figure 7.** Double well dataset with (simplified) comparison space. The double well dataset is covered with boxes, we take the union of boxes as comparison space (strictly speaking, this is no comparison space since it is not a cover in the unit tangent bundle). Four cycling segments are highlighted. The comparison space structures these in three different classes, one containing the blue, one the yellow, the last one the green and purple segments.

the homology is generated by a curve that loops exactly once around the circle. By inclusion, these curves also give rise to homology classes inside of  $Y$  where we have

$$\text{im } H_1(i_{\gamma_g, r}) = \text{im } H_1(i_{\gamma_p, r}) \neq \text{im } H_1(i_{\gamma_b, r}).$$

Therefore, we detect that the green and purple segments are qualitatively similar while the blue segment is qualitatively different.

**The Cycling Signature.** Homology classes in the image of  $i_{\gamma, r}$  indicate what we informally call elementary cycling motions. By collecting the maps for all small enough radii we obtain a map of filtered topological spaces  $i_{\gamma, \bullet}$ . Passing to homology induces a map of persistence modules  $H_1(i_{\gamma, \bullet})$ . This map is central to the following definition.

**Definition 2.** The *cycling signature* of a segment  $\gamma$  of  $\Gamma$  in  $Y$  is

$$\text{Cyc}_r(\gamma, Y) = \text{im } H_1(i_{\gamma, \bullet})$$

and its *cycling rank* is the dimension of  $\text{im } H_1(i_{\gamma, \bullet})$ .

In the introduction, we denoted the cycling signature  $V(\gamma)$  and described it as a vector space valued functor. In Definition 2, the cycling signature takes values in the category of persistence modules. We introduce this inconsistency deliberately to keep the description of the experiments accessible. In reality, the object we consider in the introduction is related to the cycling signature via

$$V(\gamma) = \text{Cyc}_r(\gamma, Y),$$

where  $r$  is a chosen evaluation radius. We note that the plots in Figs. 2 to 5 are for a fixed evaluation radius  $r$  for each system. In principle, surface plots could have been used to incorporate the  $r$ -dependence. However, we chose to fix  $r$  since this allows reading off quantitative information and, importantly, small changes in  $r$  do not qualitatively affect our results (see Appendix F).

#### 4. DISCUSSION

The cycling signature is an invariant that can be assigned to any time series segment. Statistics of these signatures provide a qualitative and quantitative description of oscillations in the data. The resulting analysis is global in nature; clusters of oscillations are detectable and transitions between oscillations can be analyzed.

Even though the analysis of nonlinear time series data has a long history [13, 2, 15, 8], to the best of our knowledge, cycling signatures provide a complementary tool with two distinguishing features. First, they can be applied to general time series data without the need for prior analysis e.g. a Poincare section, identification of dominant frequencies, etc. Second, the characterization is global in the sense that it can detect multiple oscillations and relations among them.

Our approach reduces the identification of cycling behavior to linear algebra; cycling signatures are linear subspaces of  $V(\Gamma)$ . While a canonical basis would facilitate a more direct correspondence between cycling signatures and cycling motions, this does not seem to be possible. Furthermore, the linear dependence among oscillations (cf. Fig. 5) suggests that this might not be desirable. For example, the dimension of  $V(\Gamma)$  in Dadras is 5, while we observe 6 different oscillations which are all contained in a 4-dimensional subspace of  $V(\Gamma)$ . With this in mind, our pipeline was developed to analyze oscillations without the need for a canonical basis.

A key ingredient in computing  $V(\Gamma)$  is the construction of the comparison space  $Y$ . Conceptually,  $Y$  is a neighborhood in the unit tangent bundle of some invariant set. Chaotic invariant sets typically have Cantor set like structure and thus neighborhoods can have complicated topology. However, as demonstrated by our application to Lorenz, our approach allows us to work with crude neighborhoods of the invariant set and extract meaningful descriptors of the dynamics.

Cycling signatures are dependent upon several inputs: the underlying flow  $\Phi$ , the time series  $\Gamma$ , the choice of comparison space  $Y$ , the metric  $d_C$  on the sphere bundle, and the choice of thickening  $r$ . Since these inputs are not independent, a rigorous understanding of how cycling signatures change as function of perturbations of  $\Phi$ ,  $\Gamma$ ,  $Y$ ,  $d_C$ , and  $r$  or in the data setting of noisy time series is a nontrivial task that exceeds the scope of this paper. From an empirical perspective cycling signatures appear to be a robust measurement (see Appendix G for more details). Persistent homology, which is used to select  $r$ , is known to be stable with respect to perturbations [4]. As suggested in Fig. 6c and Fig. 7, the typical cycle that is identified is based on a finite time trajectory that leads to a ‘large’ loop. It is reasonable to expect that a loop of this form should be preserved under reasonable perturbations to the input.

Our new tool is particularly useful for higher dimensional systems for which visualizations are of limited use. At first glance it appears challenging to compute cycling signatures in a higher dimensional system (the complexity of homology computations depends on the number of elementary cells whose number in general scales exponentially in the dimension of state space). However, cycling signatures only require knowledge of homology on the first level,  $H_1$ . Therefore, we only need to consider 0-, 1- and 2-dimensional cells. What is more, our approach is flexible with respect to the type of cell complex we use. We thus believe that, by a suitable improvement of our computational pipeline, the treatment of systems of considerably higher dimension should be possible.

## 5. ACKNOWLEDGMENTS

This research has been supported by the German Research Foundation (DFG – Deutsche Forschungsgemeinschaft TRR109 Project ID 195170736). K.M. was partially supported by the National Science Foundation under awards DMS-1839294 and HDR TRIPODS award CCF-1934924, DARPA contract HR0011-16-2-0033, National Institutes of Health award R01 GM126555, and Air Force Office of Scientific Research under award number FA9550-23-1-0011 and FA9550-23-1-0400. K.M. was also supported by a grant from the Simons Foundation.

## APPENDIX A. COMPUTATION

**Algorithm and Implementation.** The computational results were obtained using our implementation of the cycling pipeline (see [CyclingSignatures.jl](#)). As input, our code requires time series data together with parameters describing a comparison space (see below). The code then constructs the cubical comparison space, computes its cohomology in degree one and calculates a default sphere bundle metric parameter. After these preparatory steps, the cycling signature of any given segment can be computed. This is implemented in two steps. First, a persistence diagram of the segment is computed. This yields a barcode together with a representative cycle for each bar [\[17\]](#). Second, using a combination of ideas from image persistence [\[5\]](#) and homology induced maps [\[12\]](#), the persistence diagram of the inclusion map into the comparison space is computed. This is the cycling signature.

**Data Preprocessing.** Cycling signature computations are performed in the unit tangent bundle. Therefore for each  $x_k$  of the given time series data we need an associated unit tangent vector  $y_k$ . In case the time series is generated using a known vector field  $v$ , we compute  $y_k$  by normalizing  $v(x_k)$ . We have done this for the Lorenz and Dadras dataset. In general, the underlying vector need not be known, or even exist. In this case we approximate the tangent unit vector of the solution curve by normalizing the forward finite difference  $x_{n+1} - x_n$ . We have done this for the double well dataset.

**Cubical Comparison Spaces.** We construct the comparison space  $Y$  via a preprocessing step and reuse it for each signature computation. For a  $d$ -dimensional system we choose  $Y \subset \{(x, v) \in \mathbb{R}^{2d} \mid x, v \in \mathbb{R}^d, \|v\|_\infty = 1\}$ , the  $l_\infty$  unit tangent bundle. More precisely, we begin with a covering of  $\mathbb{R}^{2d}$  by boxes of the form

$$Q_{r,k}(p, q) = \prod_{i=1}^d r[p_i - 1/2, p_i + 1/2] \times \prod_{i=1}^d \frac{1}{k}[q_i - 1/2, q_i + 1/2] \subset \mathbb{R}^{2d}$$

where  $p, q \in \mathbb{Z}^d$ .

To cover the unit tangent bundle we fix two parameters: the space box size  $r$  and the sphere box size  $s$ . More precisely, we consider the following cover of the  $l_\infty$  unit tangent bundle

$$\mathcal{Z}_{r,k} = \{Q_{r,k}(p, q) \mid p, q \in \mathbb{Z}^d, \|q\|_\infty = k\}$$

As comparison space for a dataset  $\Gamma$  we then choose  $Y = \{Q \in \mathcal{Z}_{r,k} \mid Q \cap \Gamma \neq \emptyset\}$ . The parameters  $(r, k)$  for Lorenz, double well and Dadras are  $(8, 3)$ ,  $(0.02, 3)$  and  $(4, 3)$ , respectively.

Since the cover is in the  $l_\infty$  unit tangent bundle, while the filtration is in the  $l_2$  unit tangent bundle, the map  $\gamma^r \rightarrow Y$  is the composition of a projection with an inclusion.

With this comparison space and the metric  $d_C$  with  $C = rk$ , the map  $\gamma^s \rightarrow Y$  is well-defined for  $s \leq r$ .

## APPENDIX B. DATA GENERATION

All computations were carried out in Julia [\[1\]](#), differential equations were integrated using DifferentialEquations.jl [\[18\]](#).

**B.1. Lorenz System.** The Lorenz system [14] is a classical system of differential equations which exhibits a characteristic chaotic attractor. The equations are

$$\begin{aligned}\dot{x} &= \sigma(y - x), \\ \dot{y} &= x(\rho - z) - y, \\ \dot{z} &= xy - \beta z.\end{aligned}$$

where  $\sigma = 10$ ,  $\rho = 28$  and  $\beta = \frac{8}{3}$ .

The time series was generated by numerically integrating the equation using the Tsit5 scheme [21] with initial condition  $(0, 10, 0)$  and step size control such that two subsequent time series points have distance less than 1.

**B.2. Perturbed Double Well.** We consider a stochastically perturbed system of the form

$$(3) \quad dx = f(x)dt + \sigma dW,$$

with  $\sigma = 0.015$  and  $W$  denoting the Wiener process.

The vector field  $f$  comes from a double well Hamiltonian system which was modified to be asymmetric, have stable homoclinic orbits and is stochastically perturbed. It is given by

$$\begin{aligned}f_1(x) &= H_y(x) - 0.02h(H(x))H_x(x) \\ f_2(x) &= -H_x(x) - 0.02h(H(x))H_y(x)\end{aligned}$$

where  $h(x) = (x^3 - x)/2$  and  $H(x, y) = y^2/2 + x^4/8 - x^2/2 - x^3/15 - x/10$ .

The time series was generated by integrating (3) using the SRIW1 scheme [20] with the initial value  $x = (1, 0.75)$  and step size 0.01.

**B.3. Dadras System.** In [7], the authors consider a 4d system of differential equations with a single equilibrium at the origin and a 4 wing hyperchaotic attractor. The equations are

$$\begin{aligned}\dot{x} &= ax - yz + w, \\ \dot{y} &= xz - by, \\ \dot{z} &= xy - cz + xw \\ \dot{w} &= -y\end{aligned}$$

where we set  $(a, b, c) = (8, 40, 14.9)$  as suggested in the original article. In order to confine the system close to the origin, we use the nonlinear rescaling  $x \mapsto x/\sqrt{\|x\|}$  for all time series points.

The time series was generated by numerically integrating the equation using the Tsit5 scheme [21] with initial condition  $(10, 1, 10, 1)$  and step size control such that two subsequent time series points have distance less than 0.8.

**B.4. Runtimes.** Run times for cycling signature computations. For each system, and each length lengths  $L \in \{10, 20, \dots, 1000\}$ , we compute 1000 signatures.

System	Runtime (min)
Lorenz	17
double well	51
Dadras	60

## APPENDIX C. LORENZ RANK 1 SEGMENTS

We identified three oscillations in the Lorenz data set. An oscillation corresponds to a frequently measured rank 1 signature. For each oscillation, Fig. 8 shows a segment with the corresponding rank 1 signature. As expected, the three oscillations correspond to the outward spiraling motion on the left and right wings, and the figure 8 like motion between both wings.

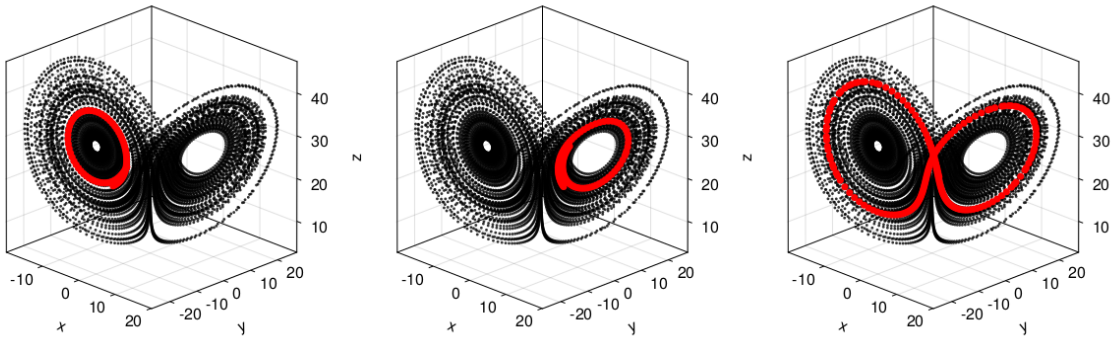


**Figure 8.** Rank 1 segments for the three oscillations in the Lorenz system. The red points in each figure highlight a segment with signature  $v_1$ ,  $v_2$  and  $v_3$ , respectively. A longer segment (black points) of the full Lorenz time series data  $\Gamma$  is plotted to outline the attractor.

It can be seen in the figure that our classification of segments is very coarse; all trajectories on orbiting the same wing are identified. This is even more obvious in Fig. 9 and, for Dadras in Fig. 10, where we see that entire ‘‘bands’’ of trajectory segments are assigned the same signature. Still, the information captured recovers important features of the underlying structure in a topologically meaningful way.

## APPENDIX D. EQUILIBRIA AND COMPARISON SPACES

The Dadras system has 4 short oscillations and 2 long oscillations which are topological ‘‘sums’’ of the shorter ones. It may therefore be unexpected that the comparison space of the system has  $\beta_1(Y) = 5$ , i.e.  $Y$  has five one dimensional holes. An analysis of the comparison space reveals that 4 of these holes correspond to centers of rotation (just like in Lorenz) while the fifth hole is generated by the saddle point at the origin. The reason for this is that close to a hyperbolic equilibrium point, points opposite of

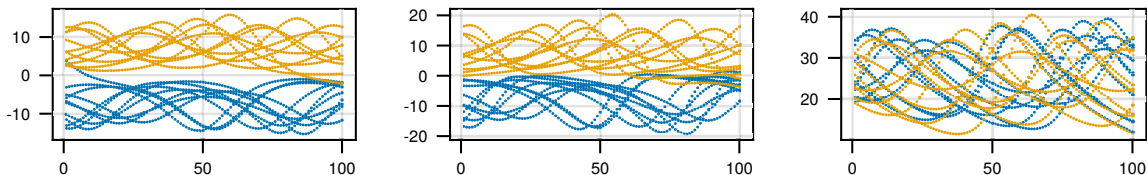


**Figure 9.** Component of cycling segments in Lorenz. Each plot shows a component of  $\Gamma_i(t)$ ,  $i = 1, 2, 3$ , for 10 cycling segments with signatures  $v_1$  and  $v_2$ . All segments have length 100.

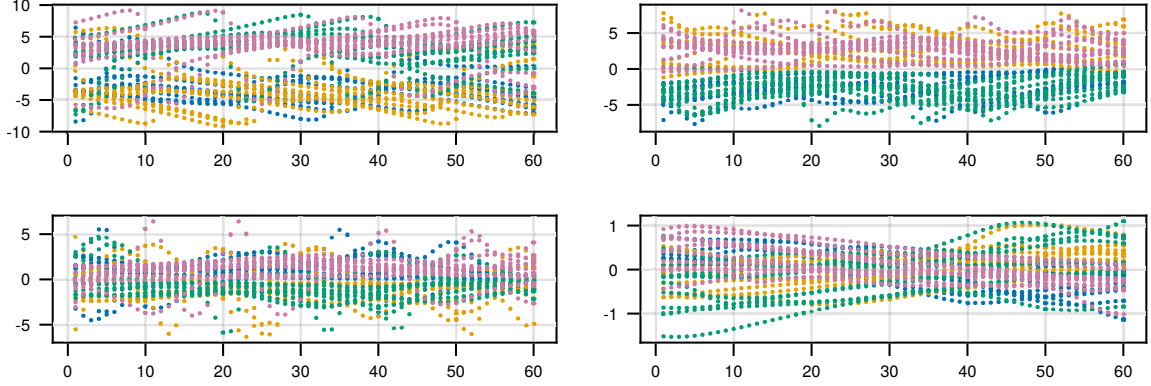


**Figure 10.** Component of cycling segments in Dadras. Each plot shows a component of  $\Gamma_i(t)$ ,  $i = 1, 2, 3, 4$ , for 5 cycling segments with signature  $v_1, \dots, v_4$ . All segments have length 50.

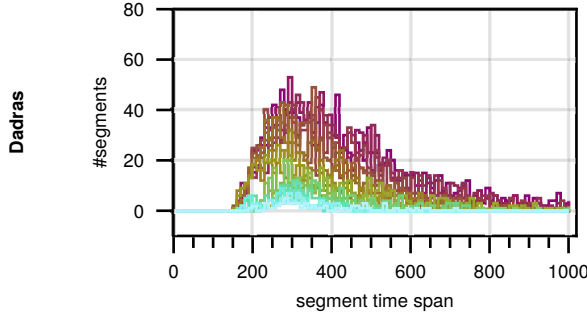


**Figure 11.** Rank 3 signatures in the Dadras system.

the equilibrium move in opposite direction and are therefore far apart in a sphere bundle metric. A similar effect occurs in the double well where the origin is a hyperbolic equilibrium of the unperturbed system.

#### APPENDIX E. DADRAS RANK 3 SEGMENTS

Rank 1 and 2 signatures of the Dadras dataset reveal six oscillations that are organized into two Lorenz like clusters. The complexity in the system becomes apparent when visualizing the distributions of rank 3 signatures (see Fig. 11). In contrast to ranks 1 and 2, a large number of rank 3 signatures appear with significant frequency. Furthermore, there is no apparent gap between distribution curves that could be used to separate relevant subspaces from noise. An interpretation of this is that after leaving one of the Lorenz-like clusters, the trajectory encounters a transition area where the next oscillation is selected at random.

#### APPENDIX F. DEPENDENCE ON EVALUATION RADIUS

For each example system, a collection of  $100 \times 1000$  cycling signatures are calculated. Each signature is a persistence module. For Figs. 2 to 4, we select, for each system, an evaluation radius  $\bar{r}$  (for Lorenz  $\bar{r} = 5$ , for double well  $\bar{r} = 0.18$ , for Dadras  $\bar{r} = 1.5$ ) and

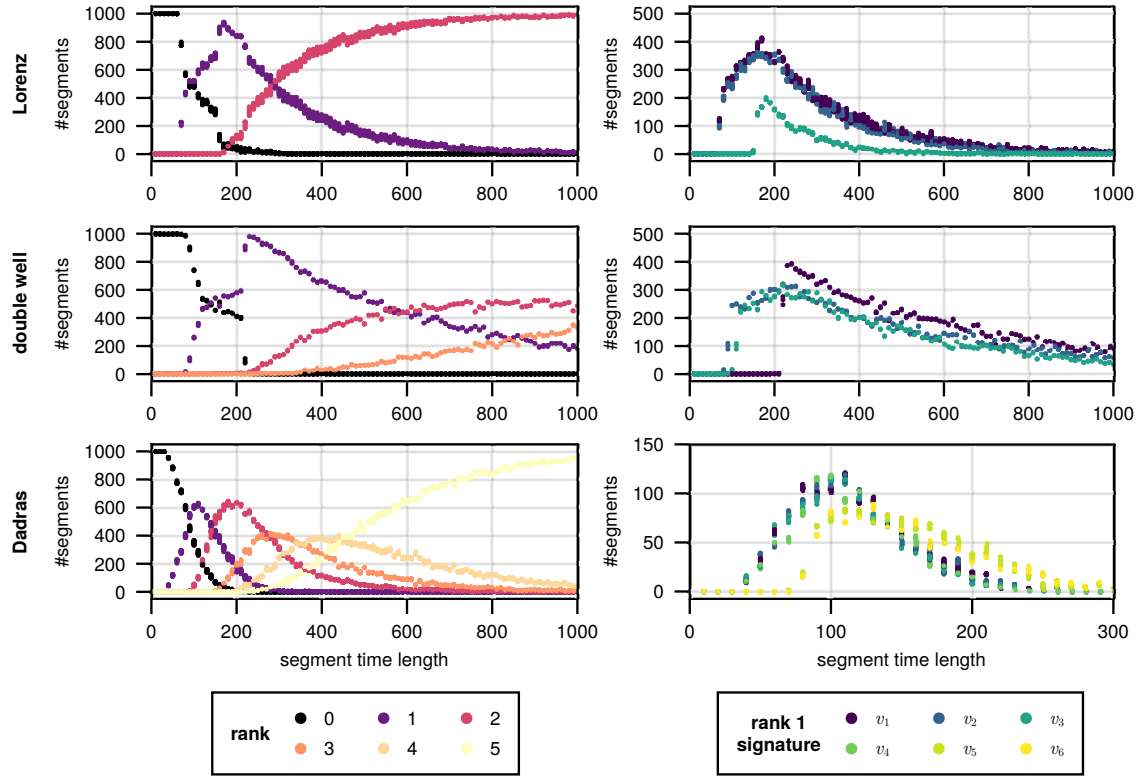


**Figure 12.** Dependence on evaluation radius. For each system, we plot the rank curves and rank 1 signature curves for 21 evaluation radii  $r$  in a neighborhood of the actual evaluation radius  $\bar{r}$ , where for Lorenz  $r \in [4.5, 5.5]$ , for double well  $r \in [0.16, 0.20]$ , for Dadras  $r \in [2.3, 2.5]$ .

consider the collection of vector spaces resulting from evaluating the cycling signatures in  $\bar{r}$ .

We verify (cf. Fig. 12) that in our experiments small changes in the evaluation radii  $r$  do not qualitatively affect Figs. 2 and 3. In general however, stability with respect to the choice of a single radius cannot be expected, since homology becomes stable only when a suitable filtration parameter is added (as in persistent homology).

#### APPENDIX G. LORENZ STABILITY EXPERIMENTS

We repeated the Lorenz experiment with small variations and experimentally investigate the effect of small parameter changes on the presented results. We consider the following parameters

- initial condition for integration:

$$\{(0, y, 0) \mid y = 9.1, 9.2, \dots, 10\}$$

- cover parameters:  $(6, 3), (7, 3), (8, 3)$ ,
- metrics  $d_C$  with  $C = 18, 21, 24$ .

For each combination of parameters, we randomly sample 1000 segments for length scales  $\{10, 20, \dots, 500\}$ . We then investigate the changes in the rank distribution for variations in each of the parameters in Figs. 13 to 15. In Figs. 16 and 17 we investigate the stability of rank 1 signatures with respect to changing initial condition.

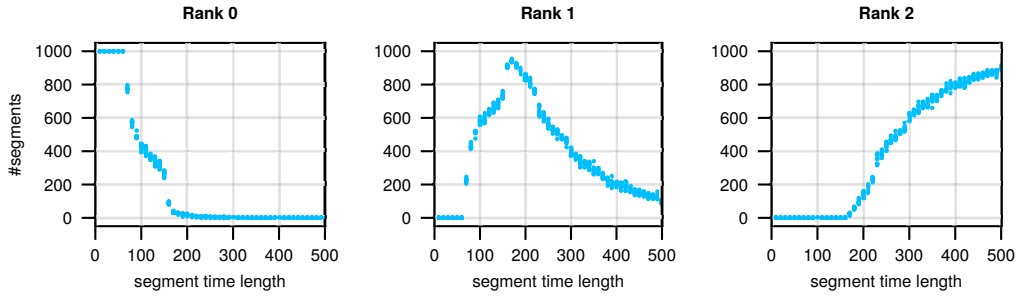


**Figure 13.** Rank frequency curves (at  $r = 6$ ) for different initial condition, the cover parameter is  $(8, 3)$  and  $C = 8$ .

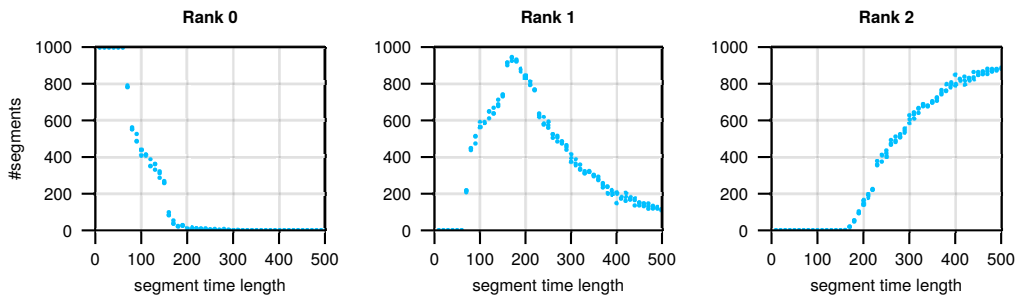


**Figure 14.** Rank frequency curves (at  $r = 6$ ) for different cover parameters. The initial condition is  $(0, 9.1, 0)$  and  $C = 8$ .

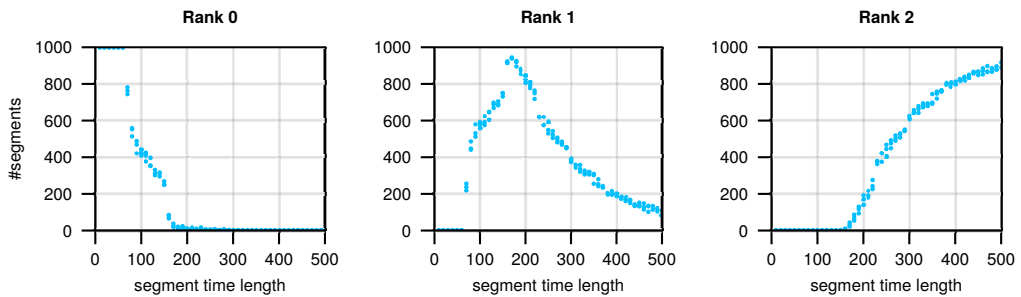


**Figure 15.** Rank frequency curves (at  $r = 6$ ) for different choices of  $C$ . The initial condition is  $(0, 9.1, 0)$ , the cover parameter is  $(8, 3)$ .

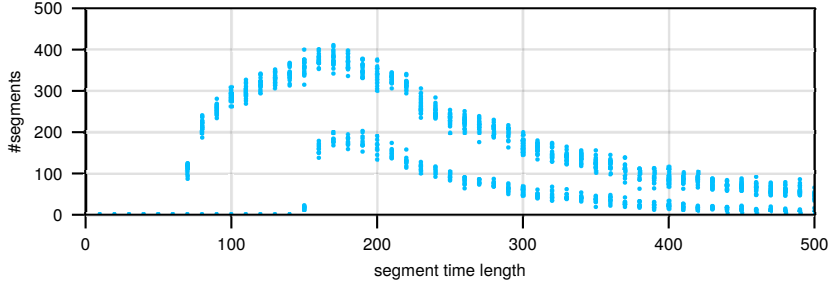


**Figure 16.** Frequency curves of rank 1 signatures (at  $r = 6$ ) for different initial conditions. The cover parameter is  $(8, 3)$  and  $C = 8$ . There are three curves per initial condition, one for each signature.

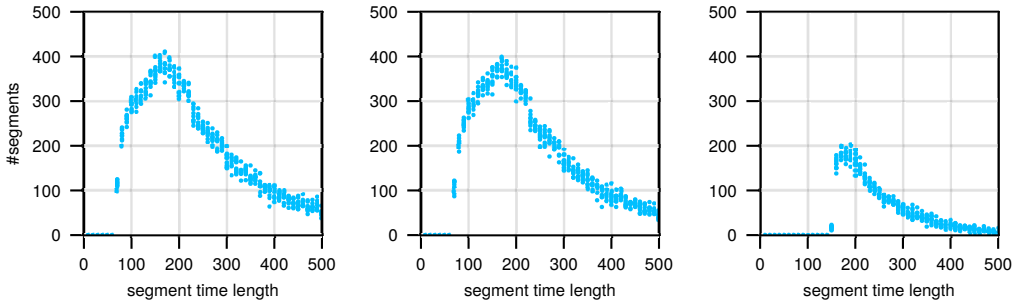


**Figure 17.** Frequency curves of rank 1 signatures (at  $r = 6$ ). The cover parameter is  $(8, 3)$  and  $C = 8$ . For each initial condition, the resulting signatures were sorted by total frequency (i.e. integral) and then plotted from left to right. Therefore, the left plot contains the frequency of the most common signature for each initial condition, the right plot the frequency of the least common signature for each initial condition.

#### APPENDIX H. RELATION TO CHAIN RECURRENCE

Conceptually, our approach has connections to the classical notion of chain recurrence [6]. Thickening a time series segment  $\gamma$  to  $\gamma^r$  can be interpreted as relaxing the deterministic evolution rule

if the system is in state  $x_k$  at time  $t_k$ , it will be in state  $x_{k+1} = \Phi(t_{k+1}, x)$  at time  $t_{k+1}$

to

if the system is in state  $x_k$  at time  $t_k$ , it will be in the ball with radius  $r$  around the state  $x_{k+1} = \Phi(t_{k+1}, x)$  at time  $t_{k+1}$ . (\*)

In this perturbed model, the evolution of the system is no longer uniquely determined, but rather any sequence  $(x_k, x_{k+1}, \dots, x_\ell)$  which satisfies  $(*)$ , called an  $r$ -chain, is a possible motion of the system. This relaxed model takes into account that any real world system is (i) subject to (unmodeled) perturbations and (ii) can only be observed with finite precision.

In contrast to our approach, there is no requirement on the topology of a chain in order for it to be considered cycling: An  $r$ -chain  $(x_k, x_{k+1}, \dots, x_\ell)$  is *periodic*, if  $x_k = x_\ell$ .

A more general notion is *r-recurrence*: We say that an *r-chain*  $(x_k, \dots, x_\ell)$  *connects* two states  $x, y$ , writing  $x \rightarrow y$ , if  $x = x_k$  and  $y$  is in the *r-ball* around  $x_\ell$ . If  $x \rightarrow y$  and  $y \rightarrow x$  then these two states are *r-chain recurrent* (or simply recurrent) and we write  $x \sim y$ . In fact, this defines an equivalence relation on the set of all recurrent states in  $X$ . The equivalence classes are the *r-chain recurrent sets*. Any state which is not recurrent lies on some chain connecting two recurrent sets, this is Conley's fundamental decomposition theorem [6, 19].

This characterization, however, is not completely satisfactory: It does not give any information on the motion of some recurrent state beyond its recurrence. In many systems, though, the dynamical behaviour within a recurrent set shows some clear structures. For example, the motion in the Lorenz system consists of two macroscopic oscillations – and this is what we capture by the new notion of cycling signatures.

## REFERENCES

- [1] Jeff Bezanson, Alan Edelman, Stefan Karpinski, and Viral B Shah. Julia: A fresh approach to numerical computing. *SIAM Review*, 59(1):65–98, 2017.
- [2] Elizabeth Bradley and Holger Kantz. Nonlinear time-series analysis revisited. *Chaos: An Interdisciplinary Journal of Nonlinear Science*, 25(9), April 2015.
- [3] Gunnar Carlsson. Topology and data. *Bull. Amer. Math. Soc. (N.S.)*, 46(2):255–308, 2009.
- [4] David Cohen-Steiner, Herbert Edelsbrunner, and John Harer. Stability of persistence diagrams. *Discrete & Computational Geometry*, 37(1):103–120, December 2006.
- [5] David Cohen-Steiner, Herbert Edelsbrunner, John Harer, and Dmitriy Morozov. Persistent homology for kernels, images, and cokernels. In *Proceedings of the Twentieth Annual ACM-SIAM Symposium on Discrete Algorithms*. Society for Industrial and Applied Mathematics, January 2009.
- [6] Charles Conley. *Isolated invariant sets and the Morse index*, volume 38 of *Reg. Conf. Ser. Math.* American Mathematical Society (AMS), Providence, RI, 1978.
- [7] Sara Dadras, Hamid Reza Momeni, Guoyuan Qi, and Zhong-lin Wang. Four-wing hyperchaotic attractor generated from a new 4d system with one equilibrium and its fractional-order form. *Nonlinear Dynamics*, 67(2):1161–1173, 2012.
- [8] Vin de Silva, Dmitriy Morozov, and Mikael Vejdemo-Johansson. Persistent cohomology and circular coordinates. *Discrete Comput. Geom.*, 45(4):737–759, 2011.
- [9] Herbert Edelsbrunner and John Harer. Persistent homology—a survey. In *Surveys on discrete and computational geometry*, volume 453 of *Contemp. Math.*, pages 257–282. Amer. Math. Soc., Providence, RI, 2008.
- [10] Robert Ghrist. Barcodes: The persistent topology of data. *Bulletin of the American Mathematical Society*, 45:61–75, 2007.
- [11] John Guckenheimer and Philip Holmes. *Nonlinear oscillations, dynamical systems, and bifurcations of vector fields*, volume 42 of *Appl. Math. Sci.* Springer, Cham, 1983.
- [12] T. Kaczynski, K. Mischaikow, and M. Mrozek. *Computational Homology*. Applied Mathematical Sciences. Springer New York, 2004.
- [13] Holger Kantz and Thomas Schreiber. *Nonlinear time series analysis*, volume 7. Cambridge university press, 2004.
- [14] Edward N. Lorenz. Deterministic nonperiodic flow. *J. Atmos. Sci.*, 20(2):130–141, 1963.
- [15] Norbert Marwan, M. Carmen Romano, Thiel Marco, and Jürgen Kurths. Recurrence plots for the analysis of complex systems. *Physics Reports*, 438(5–6):237–329, January 2007.
- [16] James R. Munkres. *Elements of Algebraic Topology*. Addison Wesley Publishing Company, 1984.
- [17] Nina Otter, Mason A Porter, Ulrike Tillmann, Peter Grindrod, and Heather A Harrington. A roadmap for the computation of persistent homology. *EPJ Data Science*, 6(1), August 2017.
- [18] Christopher Rackauckas and Qing Nie. Differentialequations.jl—a performant and feature-rich ecosystem for solving differential equations in Julia. *Journal of Open Research Software*, 5(1):15, 2017.

- [19] Clark Robinson. *Dynamical systems*. Studies in Advanced Mathematics. CRC Press, Boca Raton, FL, second edition, 1999. Stability, symbolic dynamics, and chaos.
- [20] Andreas Rößler. Runge–Kutta methods for the strong approximation of solutions of stochastic differential equations. *SIAM Journal on Numerical Analysis*, 48(3):922–952, January 2010.
- [21] Ch. Tsitouras. Runge–kutta pairs of order 5(4) satisfying only the first column simplifying assumption. *Computers & Mathematics with Applications*, 62(2):770–775, 2011.
- [22] Afra Zomorodian and Gunnar Carlsson. Computing persistent homology. *Discrete Comput. Geom.*, 33(2):249–274, 2005.

<sup>1</sup> SCHOOL OF COMPUTATION, INFORMATION AND TECHNOLOGY, TECHNICAL UNIVERSITY OF MUNICH, 85748 GARCHING, GERMANY

<sup>2</sup> MUNICH DATA SCIENCE INSTITUTE, TECHNICAL UNIVERSITY OF MUNICH, 85748 GARCHING, GERMANY

<sup>3</sup> DEPARTMENT OF MATHEMATICS, RUTGERS, THE STATE UNIVERSITY OF NEW JERSEY, 110 FRELINGHUSEN RD., PISCATAWAY, NJ 08854-8019, USA